RESEARCH ARTICLE | JUNE 09 2026

Investigation of electronic and optical properties in bismuth/antimony co-doped methylammonium lead bromide

David Machiri ; Gloria Mule ; Wycliffe Isoe ; Yusuf Madallah ; Celline Awino ; Francis M. Gaitho ; Henry Wafula ; Maxwell Mageto ; Boniface Ndinya ; Victor Odari

AIP Advances 16, 065205 (2026)
https://doi.org/10.1063/5.0306180

Investigation of electronic and optical properties in bismuth/antimony co-doped methylammonium lead bromide

Cite as: AIP Advances 16, 065205 (2026); doi: 10.1063/5.0306180
Submitted: 9 October 2025 • Accepted: 22 May 2026 •
Published Online: 9 June 2026

David Machiri,[1,a] Gloria Mule,[2] Wycliffe Isoe,[1,3] Yusuf Madallah,[1] Celline Awino,[1,3] Francis M. Gaitho,[1,3] Henry Wafula,[1,3] Maxwell Mageto,[1,3] Boniface Ndinya,[1,3] and Victor Odari[1,3]

AFFILIATIONS

[1] Department of Physics, Masinde Muliro University of Science and Technology, P.O. Box 190-50100, Kakamega, Kenya
[2] Department of Mathematics, Physics and Computing, Moi University, P.O. Box 3900-30100, Eldoret, Kenya
[3] Materials Research Society of Kenya, P.O. Box 15653-00503, Nairobi, Kenya

[a] **Author to whom correspondence should be addressed:** davidmachirin@gmail.com

ABSTRACT

Lead halide perovskites, exemplified by methylammonium lead bromide ($MAPbBr_3$), represent a cornerstone in the pursuit of next-generation photovoltaic materials owing to their tunable optoelectronic properties, defect tolerance, and cost-effective synthesis. However, their intrinsic bandgap limitations and carrier recombination pathways necessitate advanced doping strategies to enhance performance. Herein, density functional theory calculations were employed, utilizing the Perdew–Burke–Ernzerhof functional for structural optimization and the Heyd–Scuseria–Ernzerhof hybrid functional for precise electronic structure determination. Computations were conducted in a $2 \times 2 \times 2$ cubic supercell, probing a spectrum of substitutional configurations at Pb^{2+} sites, including single-dopant systems ($MAPb_{0.875}Sb_{0.125}Br_3$ and $MAPb_{0.875}Bi_{0.125}Br_3$) and co-doped variants up to high concentrations, such as $MAPb_{0.5}Sb_{0.125}Bi_{0.375}Br_3$ and $MAPb_{0.5}Sb_{0.375}Bi_{0.125}Br_3$. Band structures, interpolated via maximally localized Wannier functions using the selected columns of the density matrix with k-point sampling method, reveal a pristine direct bandgap of 2.32 eV at the Γ point, which narrows non-rigidly upon doping due to the introduction of deep donor states from heterovalent Sb^{3+} and Bi^{3+} impurities. These states manifest as midgap impurity bands, shifting the conduction band minimum downward while preserving valence band integrity. Optical properties, derived from time-dependent density functional perturbation theory via the Lanczos recursion algorithm, exhibit a pronounced redshift in the absorption onset and an enhanced intensity in the imaginary dielectric function (ε_2) across the visible spectrum, attributed to broadened interband transitions and synergistic dopant-induced polarizability. Formation energy calculations confirm the thermodynamic accessibility of these co-doped configurations.

I. INTRODUCTION

Organic–inorganic hybrid perovskites have emerged as a transformative class of semiconducting materials, attracting intense attention in recent years due to their exceptional optoelectronic properties, low-cost synthesis, and remarkable tunability through compositional engineering.[1–4] Among them, methylammonium lead bromide ($MAPbBr_3$) is notable for its superior photoluminescence quantum yield, excellent charge carrier mobility, and intrinsic stability under ambient conditions compared to its iodide-based counterparts.[5–7] Despite these advantages, the performance of pristine $MAPbBr_3$ remains constrained by intrinsic limitations in its band structure, defect tolerance, and carrier recombination dynamics.[8,9] Targeted cation or anion substitution has emerged as a promising route to overcome these shortcomings, enabling fine-tuning of the electronic structure to achieve enhanced optical absorption, extended carrier lifetimes, and improved thermal stability.[10] In particular, the isovalent substitution of lead (Pb^{2+}) with heavier elements has garnered increasing interest due to its ability to modulate bandgap characteristics and defect energetics without severely disrupting the host crystal lattice.[11]

Recent advances in perovskite solar cell technology have demonstrated significant improvements through strategic doping approaches aimed at enhancing electronic and optical properties. Various single dopant systems have been extensively investigated, with antimony (Sb^{3+}) doping showing particular promise in improving open circuit voltage and achieving high-efficiency solar cells through bandgap engineering and structural optimization.[12] Similarly, manganese (Mn) doping has demonstrated improvements in structural and optical properties.[13] Copper (Cu) ion implantation has also been explored as a strategy for developing highly efficient $MAPbBr_3$ perovskite solar cells.[14] In addition, tungsten dopant incorporation has been investigated for bandgap and type engineering of perovskite crystals, contributing to the optimization of photovoltaic performance.[15] Bismuth doping in $MAPbBr_3$ has shown mixed results, with studies demonstrating improved electron trapping capabilities while raising concerns about increased energetic disorder and charge carrier mobility reduction.[16] However, controlled low-level bismuth (Bi^{3+}) incorporation (less than 0.4%) has been found to enhance both stability and power conversion efficiency through bandgap lowering and improved visible light absorption.[17] The heterovalent nature of Bi^{3+} doping has been particularly noteworthy for its ability to induce structural modifications that enhance near-infrared photoluminescence without significantly altering fundamental electronic properties.[18,19] Despite these promising optical enhancements, bismuth doping faces challenges related to the formation of donor-yielded complex centers that act as deep electron traps, potentially limiting n-type doping effectiveness and carrier lifetimes.[20] Experimental studies have further revealed that while Bi^{3+} doping maintains the fundamental bandgap of $MAPbBr_3$, it introduces blueshifted photoluminescence and enhanced Urbach tails, indicating increased structural disorder.[21,22] The broader context of heterovalent doping strategies has demonstrated the potential for precise bandgap and carrier type engineering in perovskite crystals,[23] with metal-doped lead halide perovskites showing enhanced optoelectronic properties.[11] Past research on Sb^{3+} and Bi^{3+} codoping has indicated promising improvements in structural, optical, and photovoltaic properties, with optimized energy gap and refractive index relationships.[24,25]

The success of these individual doping strategies on $MAPbBr_3$ has laid the foundation for exploring more complex doping schemes. While individual doping strategies have shown considerable promise, a comprehensive understanding of synergistic effects in bismuth–antimony codoping systems remains limited, presenting an opportunity for a systematic theoretical investigation of the effects of codoping on electronic and optical properties of $MAPbBr_3$ perovskites. This knowledge gap is particularly significant given that cooperative dopant effects can induce non-trivial modifications in the electronic and optical responses. Most prior theoretical studies have relied solely on semilocal density functional theory (DFT) approaches, which, although computationally efficient, notoriously underestimate bandgaps and fail to capture subtle hybridization effects that strongly influence optoelectronic performance.

We present a comprehensive first-principles study of pristine and Bi^{3+}–Sb^{3+} co-doped $MAPbBr_3$ using a combination of the Perdew–Burke–Ernzerhof (PBE) functional for structural optimization and the Heyd–Scuseria–Ernzerhof (HSE) hybrid functional for accurate electronic structure determination. Optical properties were computed using the thermo_pw package within the Quantum ESPRESSO suite, employing time-dependent density functional perturbation theory (TD-DFPT) in conjunction with the Lanczos recursion algorithm to capture excitonic and many-body effects efficiently. By systematically varying the degree of Bi^{3+} and Sb^{3+} substitution at Pb^{2+} sites in a $2 \times 2 \times 2$ cubic supercell, we investigate how codoping influences the band structure and optical absorption spectra. Our findings reveal distinct cooperative effects in Bi^{3+}–Sb^{3+} co-doped systems, including notable bandgap tuning, enhanced visible-light absorption, and a potential pathway for improving photoconversion efficiency in lead-reduced halide perovskite technologies. While experimental studies have demonstrated optimal performance at low doping levels (<0.4%),[17] the present theoretical investigation systematically explores higher concentrations to elucidate fundamental electronic structure modifications and establish concentration-dependent trends. These high-concentration calculations serve to amplify dopant-induced effects, facilitating detailed analysis of charge compensation mechanisms, impurity band formation, and spin–orbit coupling phenomena that inform our understanding across all doping regimes. This work not only advances the fundamental understanding of dopant-induced modifications in hybrid perovskites but also provides a theoretical blueprint for the rational design of next-generation optoelectronic materials.

II. COMPUTATIONAL DETAILS

First-principles calculations were performed within the framework of DFT using the Quantum ESPRESSO package.[26–28] The exchange–correlation energy was initially treated within the PBE parameterization of the generalized gradient approximation (GGA),[29] with norm-conserving pseudopotentials employed in a fully self-consistent plane-wave basis. A kinetic energy cutoff point of 80Ry and a Monkhorst–Pack k-point grid of $3 \times 3 \times 3$ were used.[30] All atomic structures were relaxed until the forces were below 0.03 eV/Å, and all systems were treated in their cubic perovskite phase shown in Fig. 1.[31] Structural optimization was performed by relaxing atomic positions while maintaining the overall lattice symmetry. This approach enables consistent comparison across doping

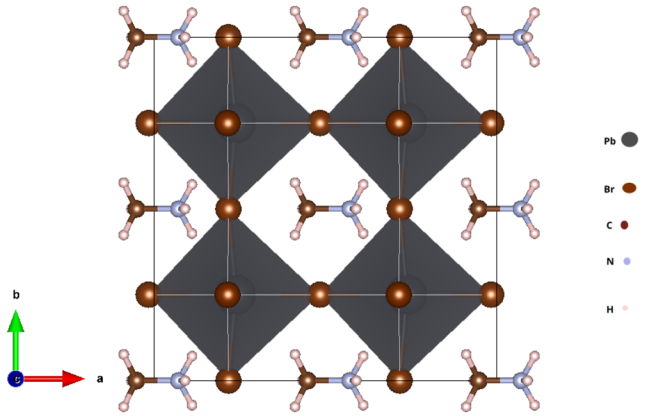

FIG. 1. The $2 \times 2 \times 2$ cubic supercell of $MAPbBr_3$. Structure based on crystallographic data from Ref. 31 (GNU GPL v2.0).

concentrations but may underestimate local distortions such as octahedral tilting induced by heterovalent dopants. Nevertheless, the observed trends in electronic and optical properties remain physically meaningful within this regime. The doping ratios investigated in this study were achieved through the systematic substitution of Sb^{3+} and Bi^{3+} atoms at Pb^{2+} sites within a $2 \times 2 \times 2$ supercell of the cubic $MAPbBr_3$ perovskite structure. This supercell, comprising 96 atoms including 8 Pb^{2+} sites, enabled precise control over dopant concentrations, with each substitution corresponding to an incremental fraction of 0.125. Initial single-dopant configurations involved replacing one Pb^{2+} atom with Sb^{3+} or Bi^{3+}, yielding $MAPb_{0.875}Sb_{0.125}Br_3$ and $MAPb_{0.875}Bi_{0.125}Br_3$, respectively. For co-doped systems, combinations of Sb^{3+} and Bi^{3+} substitutions were explored to assess synergistic effects. These concentrations were selected to enable a systematic theoretical investigation of electronic band structure modifications and optical property enhancements within computationally accessible supercell dimensions.

To obtain more accurate bandgap estimates and capture the electronic structure with greater precision, screened hybrid functional calculations were performed using the HSE approach.[32] However, given the high computational demand for hybrid functionals for large supercells (96 atoms in our $2 \times 2 \times 2$ $MAPbBr_3$ supercell), we employed an interpolation scheme based on maximally localized Wannier functions (MLWFs) as implemented in the Wannier90 code.[33–35] The initial projections for Wannierization were obtained using the Selected Columns of the Density Matrix with k-point sampling (SCDM-k) method.[36,37]

The optical properties were calculated using the Thermo_pw post-processing suite within the Quantum ESPRESSO package.[26,27] The frequency-dependent dielectric function was obtained from first principles via TD-DFPT.[38] This approach accounts for many-body effects in the linear optical response beyond the independent-particle approximation.[39] To efficiently compute the macroscopic dielectric function over a broad frequency range, we employed the Lanczos recursion algorithm, which enables accurate spectral resolution without the need to explicitly calculate a large number of unoccupied states.[40,41]

The heterovalent substitution of divalent Pb^{2+} with trivalent Sb^{3+} and Bi^{3+} dopants introduces excess positive charge; in the present calculations, charge compensation is achieved through electronic doping, where the excess positive charge is balanced by additional electrons occupying states near the conduction band minimum.[42] This is handled automatically within the Quantum ESPRESSO framework through the adjustment of the number of valence electrons to match the total ionic charge of the supercell. This electronic compensation mechanism is physically reasonable for n-type doping scenarios. The focus of this study is on intrinsic electronic structure modifications arising from cation substitution under the assumption of ideal n-type electronic doping.

The thermodynamic stability of doped configurations was evaluated through defect formation energies calculated as[43]

$$E_f = E_{doped} - E_{pristine} - \sum n_i \mu_i, \quad (1)$$

where E_{doped} and $E_{pristine}$ represent the total energy of the doped and pristine supercells, respectively, n_i is the number of atoms of species i exchanged, and μ_i is the chemical potential referenced to the elemental bulk phase (FCC Pb and rhombohedral Sb and Bi). Bulk reference energies were computed using identical computational parameters with $10 \times 10 \times 10$ k-point sampling.

III. RESULTS AND DISCUSSION

A. Electronic band structure analysis

The electronic band structures obtained from HSE hybrid functional calculations followed by Wannierization using the SCDM-k method reveal significant modifications in the electronic properties of $MAPbBr_3$ upon Bi and Sb doping. Figure 2(a) shows the pristine $MAPbBr_3$ band structure, which exhibits a direct bandgap of 2.32 eV at the Γ point, consistent with the cubic perovskite phase. The valence band maximum (VBM) is set as the energy reference, and the conduction band minimum (CBM) displays the characteristic dispersion of lead halide perovskites. Doping introduces band folding and symmetry breaking, manifesting as increased band multiplicity and dispersion variations. The observed energy-level shifts are predominantly non-rigid: the VBM remains anchored as the reference, while the CBM shifts downward, narrowing the gap through the extension of donor-induced tail states into the forbidden region. This non-rigid behavior arises from electrostatic potentials generated by positively charged dopant sites, which lower nearby energy levels. Critical examination of the conduction band regions in the doped systems reveals the emergence of additional electronic states that were absent in the pristine $MAPbBr_3$ structure. These states, clearly visible in Figs. 2(b)–2(d), are positioned within the conduction band minimum and represent donor levels introduced by the heterovalent doping process. The formation of these states can be understood through charge compensation arguments, and the substitution of divalent Pb^{2+} with trivalent Sb^{3+} or Bi^{3+} introduces excess positive charge that must be electronically compensated. The consistent appearance of these donor states across all doping configurations demonstrates the effectiveness of both Sb^{3+} and Bi^{3+} as electron-donating species in the $MAPbBr_3$ lattice.[44]

A particularly noteworthy feature observed in the doped systems is the emergence of Rashba-type band splitting, most evident along the Γ–Z symmetry line in Figs. 2(b) and 2(c). This splitting arises from the combination of broken inversion symmetry due to heterovalent substitution and the strong spin–orbit coupling (SOC) effects inherent to the heavy Bi^{3+} and Sb^{3+} atoms.[45] The Rashba splitting manifests as an energy separation between otherwise degenerate bands, creating momentum-dependent spin textures in the electronic states. This phenomenon is absent in the pristine structure, confirming its origin from the dopant-induced perturbations to the crystal symmetry and electronic environment.[46] The presence of Rashba splitting has significant implications for carrier dynamics and photovoltaic performance. The momentum separation of spin states can suppress certain electron–hole recombination pathways by creating additional scattering channels that favor radiative over non-radiative processes. The splitting provides multiple pathways for electronic transitions, potentially enhancing the absorption coefficient and extending the spectral response range of the material.[47]

In Fig. 3(a), a prominent flat impurity band emerges 0.8–1.0 eV above the VBM, primarily attributable to Sb^{3+}-dominant deep donor states. These states originate from donor-yielded complex (DY) centers formed by Sb^{3+}, where the excess electron is trapped alongside compensating bromide interstitials, resulting in localized

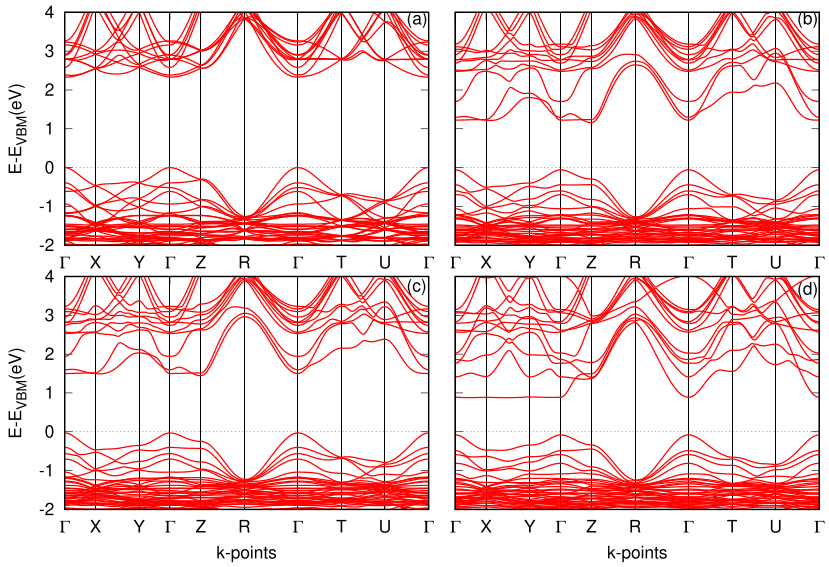

FIG. 2. Band structures of (a) $MAPbBr_3$, (b) $MAPb_{0.875}Sb_{0.125}Br_3$, (c) $MAPb_{0.875}Bi_{0.125}Br_3$, and (d) $MAPb_{0.75}Bi_{0.125}Sb_{0.125}Br_3$.

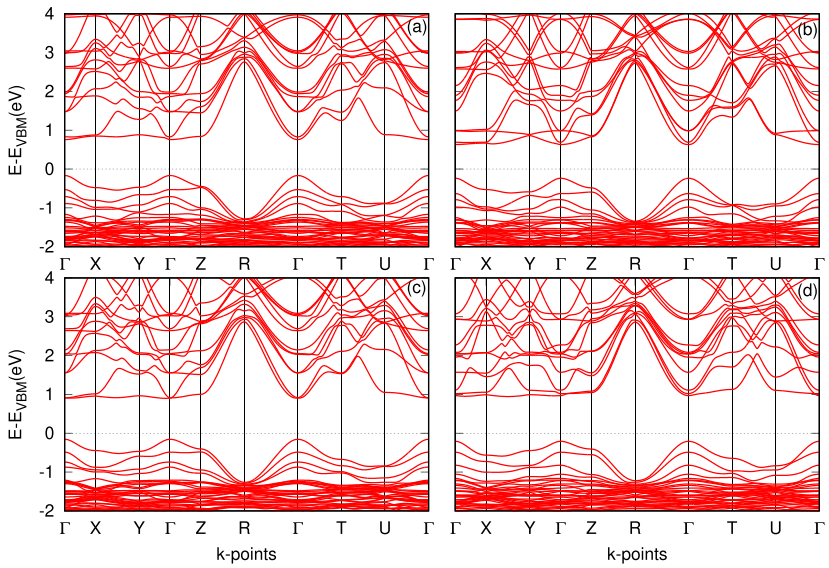

FIG. 3. Band structures of (a) $MAPb_{0.625}Bi_{0.125}Sb_{0.25}Br_3$, (b) $MAPb_{0.5}Bi_{0.125}Sb_{0.375}Br_3$, (c) $MAPb_{0.625}Bi_{0.25}Sb_{0.125}Br_3$, and (d) $MAPb_{0.5}Bi_{0.375}Sb_{0.125}Br_3$.

orbitals that hinder shallow donor behavior. The lower Bi^{3+} concentration contributes minor synergistic deep traps, enhancing near-infrared (NIR) emission without excessive disorder. Energy shifts manifest as a downward displacement of the CBM, driven by donor tail states extending into the gap, which reflects the electrostatic stabilization from charged dopants and lone-pair-induced distortions.[48] The VB exhibits slight flattening near the VBM, indicative of hole-trapping compensation, while the CB retains moderate dispersion, suggesting preserved electron mobility. Elevating the Sb^{3+} fraction, Fig. 3(b), with minimal Bi^{3+} yields a more pronounced Sb^{3+}-dominant deep donor states. Denser impurity states in the CBM form a near-continuous band, stemming from multiple Sb^{3+} induced DY centers that amplify defect density. The low Bi^{3+} content introduces selective deep traps, but the valence excess from Sb^{3+} dominates, leading to electron occupancy of these states, which decreases effective doping. The CBM downshifts prominently, accompanied by Urbach-like tails broadening the band edges. VB flattening from −1.5 to 0 eV, with avoided crossings along Z–R–Γ, signals compensatory acceptor effects. In Fig. 3(c), midgap levels are Bi^{3+}-driven deep donors, manifesting as NIR emitting traps that preserve the fundamental gap while introducing localized states. The low Sb^{3+} fraction provides compensatory shallower donors, alleviating Bi^{3+} trapping through lone-pair synergy and reduced distortions. Energy shifts include a CBM downshift from Bi^{3+} donor tails, with less edge broadening than Sb-dominant cases, reflecting localized non-rigid modifications via structural changes.[49] In Fig. 3(d), the highest Bi^{3+} concentration shows dense midgap bands that arise from Bi^{3+}'s deep donors, forming trap-rich

impurity bands due to valence excess and strain. Minimal Sb^{3+} tempers this, but electron filling of deep states prevails, promoting recombination. The CBM exhibits a strong downshift with broad tails, non-rigidly induced by Bi^{3+} electrostatic pinning. Pronounced VB flattening signals disorder. Sb^{3+}–Bi^{3+} codoping modulates donor states to achieve tunable electronic properties with balanced configurations [Figs. 3(a) and 3(c)], offering optimal synergy for enhanced stability and efficiency in perovskite solar cells.

B. Optical properties

The optical properties of Sb/Bi codoped $MAPbBr_3$, computed via TD-DFPT within the Liouville–Lanczos framework as implemented in Quantum ESPRESSO, reveal significant modifications induced by heterovalent doping. Below, we present a comparative analysis for each subplot, contrasting the pristine $MAPbBr_3$ with progressively doped samples. The real part of the inverse dielectric function, Re $1/\varepsilon(q, \omega)$, shown in Fig. 4, quantifies the screening of external fields and is sensitive to electronic polarizability. In the plotted energy range, S_A exhibits a baseline value around 0.31 at zero frequency, rising gradually to 1.0–1.2 at higher energies, indicative of weak screening in the undoped perovskite due to its ionic–covalent character. S_B shows a slight upward shift across the spectrum, with peaks sharpening around mid-range, reflecting increased polarizability from Sb^{3+}-induced donor states that enhance free-carrier contributions. S_C shows a more pronounced elevation, reaching 1.1 at peak, attributable to a Bi^{3+} larger ionic radius and stronger lone-pair effects causing greater lattice polarization. S_D combines these, yielding intermediate values (0.8–1.0), suggesting synergistic screening without excessive disorder. Increasing Sb concentration, S_E and S_F, further amplifies Re $1/\varepsilon$, with S_F displaying the highest values (1.2), due to denser donor states facilitating better charge delocalization and reduced effective gap. Conversely, bi-dominant codoping, S_G and S_H, moderates this rise, with S_H peaking at 1.0, as Bi^{3+} deep traps localize carriers, diminishing screening efficiency. Overall, codoping elevates Re $1/\varepsilon$ compared to pristine, enhancing defect tolerance for photovoltaic applications, although high Bi^{3+} fractions risk over-localization.

The electron energy loss function, $-\mathrm{Im}\ 1/\varepsilon(q, \omega)$, shown in Fig. 4, reveals collective electronic excitations and provides information about plasmon resonances. The pristine system (S_A) exhibits relatively modest energy loss features, with the primary loss peak occurring around 15–18 eV, corresponding to bulk plasmon excitations involving core electrons. Upon doping, significant modifications appear in the energy loss spectra. All doped systems show enhanced loss intensity in the 5–12 eV range, indicating increased density of electronic excitations in this energy regime. This enhancement is attributed to the additional electronic states introduced by dopant atoms and the modification of transition probabilities due to the altered electronic structure. S_B intensifies these, shifting peaks slightly leftward, indicative of increased carrier density from

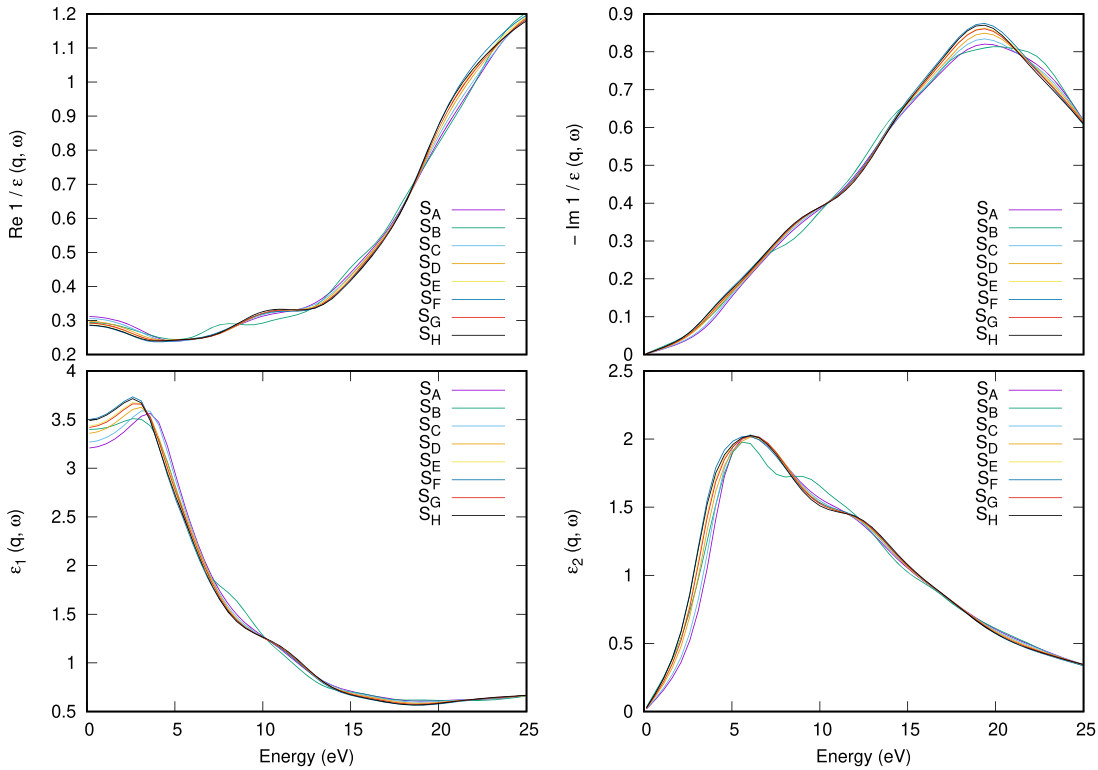

FIG. 4. Optical properties; S_A is $MAPbBr_3$, S_B is $MAPb_{0.875}Sb_{0.125}Br_3$, S_C is $MAPb_{0.875}Bi_{0.125}Br_3$, S_D is $MAPb_{0.75}Bi_{0.125}Sb_{0.125}Br_3$, S_E is $MAPb_{0.625}Bi_{0.125}Sb_{0.25}Br_3$, S_F is $MAPb_{0.5}Bi_{0.125}Sb_{0.375}Br_3$, S_G is $MAPb_{0.625}Bi_{0.25}Sb_{0.125}Br_3$, and S_H is $MAPb_{0.5}Bi_{0.375}Sb_{0.125}Br_3$.

shallow donor states enhancing plasmon damping. S_C yields sharper, higher peaks, reflecting Bi^{3+}-induced surface plasmons from localized states. S_D exhibits balanced intensification, merging Sb^{3+} delocalization with Bi^{3+} localization. In S_E and S_F, $-\mathrm{Im}\ 1/\varepsilon$ escalates progressively, with S_F reaching 0.8–0.9 and redshifted peaks, correlating with narrowed gaps and Urbach tails that broaden loss channels. S_G and S_H show similar intensification but with additional sub-peaks, suggesting multiple plasmon modes from defect clusters; S_H's maximum implies heightened losses, potentially limiting carrier lifetime. The co-doped systems (S_D through S_H) display particularly complex energy loss spectra with multiple overlapping features. These complex patterns reflect the superposition of excitations from different electronic environments created by the presence of both Sb^{3+} and Bi^{3+} dopants. Comparatively, doping increases loss function amplitude, promoting NIR plasmonics but necessitating balanced codoping to minimize non-radiative decay in solar cells.

The real part of the dielectric function $\varepsilon_1(q, \omega)$ vs photon energy illustrates electronic polarization, with the static value representing the dielectric constant (ε_r). S_A displays ε_1 starting at 3.21; this high ε_r stems from ionic contributions in $MAPbBr_3$. S_B elevates the static ε_1 to 3.8, with slower decay, due to Sb enhancing polarizability via extended orbitals. S_C further increases it to 3.26, with pronounced oscillations, linked to Bi^3 hypervalent bonding amplifying screening. S_D achieves 3.36, balancing these effects. S_E and S_F boost static ε_1 to 3.43 and 3.50, respectively, with redshifted zero-crossings, reflecting gap narrowing and donor-enhanced free-carrier screening. S_G and S_H yield 3.42 and 3.48, respectively, indicating strong plasmonic reflection from localized states. Doping universally raises ε_r over pristine, improving charge separation in photovoltaics. This enhancement in static dielectric constant is attributed to the increased polarizability introduced by the heavier Sb^3 and Bi^3 atoms, which possess more extended electron clouds and a stronger response to external electric fields.[11]

The imaginary dielectric function $\varepsilon_2(q, \omega)$ directly correlates with optical absorption, where the onset marks the fundamental bandgap and peaks arise from interband transitions. For S_A, absorption commences at 2.3 eV, peaking around 3–5 eV, and secondary maxima at 10–15 eV, consistent with pristine $MAPbBr_3$'s visible-light response. The absorption spectrum exhibits characteristic features of perovskite materials, including a sharp fundamental absorption edge followed by higher-energy transitions. Doping introduces systematic redshifts in the absorption edge that correlate with the observed band structure modifications. S_B shifts the onset to 1.9 eV with a heightened primary peak due to Sb^{3+} donor tails extending absorption into NIR. S_C exhibits a redshift with onset at 2.1 eV and intensified peaks, from Bi^{3+} deep states, facilitating sub-gap transitions. S_D combines these, with onset at 2.0 eV, demonstrating codoping synergy. S_E and S_F progressively redshift onsets to 1.7 and 1.6 eV, respectively, correlating with denser midgap states enhancing visible/NIR absorption. S_G and S_H show onsets at 1.8 and 1.7 eV, respectively, enabling light harvesting deep into the NIR region. The high-concentration systems (S_E through S_H) exhibit broadened absorption features and increased oscillator strength, indicating enhanced light–matter interaction efficiency. A particularly noteworthy feature is the enhancement in absorption intensity across the visible spectrum for all doped systems. This enhancement is most pronounced in the 1.5–3.0 eV range, which overlaps significantly with the solar spectrum. The increased absorption is attributed to the presence of donor states that create additional optical transition pathways and the relaxation of selection rules due to symmetry breaking introduced by dopant atoms.[50] Compared to pristine, doping reduces the onset and amplifies ε_2, optimizing solar spectrum matching while risking recombination in high-dopant regimes.

The observed electronic structure modifications have several favorable implications for photovoltaic applications. The systematic band structure modifications enhance the overlap with the solar spectrum, potentially improving light absorption in the visible and NIR regions. The introduction of donor states increases the electron concentration, which can improve the material's electrical conductivity and facilitate more efficient charge transport. In addition, the Rashba splitting effects may contribute to enhanced charge separation and reduced recombination rates, factors that are crucial for achieving high power conversion efficiencies. The absorption edge systematically redshifts with increasing dopant concentration, with Sb^{3+} showing stronger effects than Bi^{3+}. This trend directly correlates with the electronic band structure modifications observed in the band structure analysis. All doped systems exhibit enhanced absorption intensity in the visible and NIR regions, with the most significant improvements in systems with higher Sb^{3+} concentrations. This enhancement is crucial for photovoltaic applications as it enables more efficient solar spectrum utilization. The static dielectric constant increases systematically with doping level, reaching maximum values in the highest concentration systems. This enhancement improves the material's ability to separate photogenerated charges and reduce recombination losses. Higher doping levels introduce increasingly complex energy loss spectra, reflecting the rich electronic structure modifications and enhanced density of electronic excitations. The optical property modifications observed in the doped systems have several favorable implications for photovoltaic applications. The redshifted absorption edge combined with enhanced absorption intensity enables improved solar spectrum harvesting, particularly in the NIR region where pristine $MAPbBr_3$ shows limited response.[51] The enhanced static dielectric constant facilitates better charge separation and reduced Coulomb binding of photogenerated electron–hole pairs. The codoping strategy demonstrates particular promise, as it combines the beneficial effects of both dopants while maintaining the overall crystal structure integrity.

C. Thermodynamic stability and formation energies

Defect formation energies calculated under metal-rich conditions (Table I) reveal that all doped configurations exhibit positive E_f values, indicating thermodynamic metastability consistent with the requirement for non-equilibrium synthesis techniques. Single-dopant systems show nearly equivalent formation energies, suggesting comparable thermodynamic barriers.[52] Co-doped configurations display non-linear scaling with dopant concentration; the balanced Sb:Bi system (E_f = 0.187 eV, 0.094 eV/dopant) exhibits a linear increase relative to single-dopant values, indicating weak repulsive dopant–dopant interactions arising from cumulative strain fields.[53,54] At higher concentrations, formation energies increase systematically, with Sb-rich configurations generally showing higher

TABLE I. Formation energies for various dopant concentrations.

Composition	Total dopants	E_f (eV)	E_f per dopant (eV)
$MAPbBr_3$	0	...	...
$MAPb_{0.875}Sb_{0.125}Br_3$	1	0.055	0.055
$MAPb_{0.875}Bi_{0.125}Br_3$	1	0.058	0.058
$MAPb_{0.75}Bi_{0.125}Sb_{0.125}Br_3$	2	0.187	0.094
$MAPb_{0.625}Bi_{0.125}Sb_{0.25}Br_3$	3	0.316	0.105
$MAPb_{0.5}Bi_{0.125}Sb_{0.325}Br_3$	4	0.423	0.106
$MAPb_{0.625}Bi_{0.25}Sb_{0.125}Br_3$	3	0.290	0.097
$MAPb_{0.5}Bi_{0.325}Sb_{0.125}Br_3$	4	0.396	0.099

values than Bi-rich systems, reflecting the greater lattice strain induced by the smaller Sb^{3+} ionic radius (0.76 Å) compared to Bi^{3+} (1.03 Å). Normalized per-dopant formation energies range from 0.055 to 0.106 eV, remaining within modest magnitudes (<0.11 eV/dopant) that are accessible through kinetically controlled crystal growth methods such as rapid thermal annealing or anti-solvent precipitation.[55]

IV. CONCLUSION

In this work, Sb^{3+}–Bi^{3+} codoping modulates donor states to achieve tunable electronic and optical properties, offering optimal synergy for enhanced stability and efficiency in perovskite solar cells. These results collectively demonstrate that Bi^{3+}–Sb^{3+} codoping represents a viable strategy for engineering the electronic properties of $MAPbBr_3$ perovskites, with the potential to address key limitations of the pristine material while introducing new functionalities through SOC effects and controlled n-type doping. The systematic tunability of optical properties through dopant concentration control provides a pathway for optimizing light absorption characteristics for specific applications. Thermodynamic metastability directly enables the donor state formation and enhanced dielectric response responsible for the observed bandgap narrowing and absorption redshift. These findings demonstrate that Sb^{3+}–Bi^{3+} codoping represents a powerful strategy for engineering the optical properties of $MAPbBr_3$ perovskites, with the potential to significantly enhance photovoltaic performance through improved light harvesting efficiency and optimized electronic properties.

While our calculations reveal promising electronic and optical property enhancements at high doping concentrations, practical implementation would require optimization at significantly lower dopant levels (<1%) to maintain structural stability and perovskite phase integrity. The insights gained regarding bandgap modulation mechanisms, donor state characteristics, and Rashba splitting phenomena are expected to remain qualitatively valid at lower, experimentally relevant concentrations, although the magnitude of effects would be proportionally reduced. Future computations of defect formation energies, charge transition levels, and detailed charge density analyses will help assess thermodynamic stability and defect compensation mechanisms, thereby providing a robust theoretical framework toward stable, high-performance perovskite solar cells.

ACKNOWLEDGMENTS

The authors gratefully acknowledge the Center for High Performance Computing (CHPC), South Africa, for providing computational resources on the Lengau cluster through Project No. MATS1426. The authors also acknowledge Kenya Education Network (KENET) mini-grant 2019 to MMUST, Masinde Muliro University of Science and Technology, Grant No MMU/URF/2022/1-026, and Advanced Physics Training and Collaboration with Africa (APhRICA).

AUTHOR DECLARATIONS

Conflict of Interest

The authors have no conflicts to disclose.

Author Contributions

David Machiri: Conceptualization (equal); Data curation (lead); Formal analysis (lead); Investigation (lead); Methodology (equal); Software (equal); Visualization (lead); Writing – original draft (lead); Writing – review & editing (equal). **Gloria Mule**: Writing – review & editing (supporting). **Wycliffe Isoe**: Writing – review & editing (supporting). **Yusuf Madallah**: Writing – review & editing (supporting). **Celline Awino**: Supervision (equal); Validation (equal); Writing – review & editing (equal). **Francis M. Gaitho**: Writing – review & editing (equal). **Henry Wafula**: Writing – review & editing (supporting). **Maxwell Mageto**: Writing – review & editing (supporting). **Boniface Ndinya**: Writing – review & editing (supporting). **Victor Odari**: Conceptualization (equal); Data curation (equal); Formal analysis (equal); Funding acquisition (lead); Investigation (equal); Methodology (equal); Project administration (lead); Resources (lead); Software (equal); Supervision (lead); Validation (lead); Visualization (equal); Writing – original draft (equal); Writing – review & editing (lead).

DATA AVAILABILITY

The data that support the findings of this study are available from the corresponding author upon reasonable request.

REFERENCES

[1] Y. Du, P. Liu, F. Li, X. Hou, H. Zhang, Y. Shi, S. Wang, Y. Wang, S. Guo, Q. Tai, and X. Zhao, J. Alloys Compd. **832**, 154902 (2020).
[2] J. Luan, J. Xu, J. Chen, X. Shi, B. Zhang, S. Dai, and J. Yao, J. Solid State Chem. **270**, 436 (2019).
[3] W. S. Subhani, K. Wang, M. Du, X. Wang, N. Yuan, J. Ding, and S. F. Liu, J. Energy Chem. **34**, 12 (2019).
[4] W. Wang, M. O. Tadé, and Z. Shao, Chem. Soc. Rev. **44**, 5371 (2015).
[5] Y. Chen, L. Zhang, Y. Zhang, H. Gao, and H. Yan, RSC Adv. **8**, 10489 (2018).
[6] P. Roy, A. Ghosh, F. Barclay, A. Khare, and E. Cuce, Coatings **12**, 1089 (2022).
[7] H. Liu and X. Yang, Ferroelectrics **507**, 69 (2017).
[8] X. Dong, Y. Shen, F. Wang, Z. He, Y. Zhao, Z. Miao, and Z. Wu, Small **21**, 2412809 (2025).
[9] H. Wei and J. Huang, Nat. Commun. **10**, 1066 (2019).
[10] J. Euvrard, Y. Yan, and D. B. Mitzi, Nat. Rev. Mater. **6**, 531 (2021).

[11] Y. Zhou, J. Chen, O. M. Bakr, and H.-T. Sun, Chem. Mater. **30**, 6589 (2018).
[12] A. Attia, M. I. Khan, S. Hussain, A. Ali, A. F. Seliem, A. Y. A. Mohammed, and M. M. Ibrahim, Opt. Mater. **147**, 114611 (2024).
[13] M. I. Khan, S. Hussain, M. Boota, W. Shahid, M. Atif, and A. Nazneen, Results Opt. **15**, 100663 (2024).
[14] S. Hussain, M. I. Khan, A. Ghafoor, W. S. Subhani, W. Shahid, Z. Mahmoud, Z. M. Elqahtani, F. Ercan, N. Alwadai, and M. Iqbal, Opt. Mater. **140**, 113806 (2023).
[15] M. Khan, S. Hussain, W. S. Subhani, M. Ammami, W. Shahid, and R. Ali, Phys. Scr. **98**, 095517 (2023).
[16] A. M. Ulatowski, A. D. Wright, B. Wenger, L. R. V. Buizza, S. G. Motti, H. J. Eggimann, K. J. Savill, J. Borchert, H. J. Snaith, M. B. Johnston, and L. M. Herz, J. Phys. Chem. Lett. **11**, 3681 (2020).
[17] P.-P. Sun, D. R. Kripalani, L. Bai, and K. Zhou, J. Phys. Chem. C **123**, 12684 (2019).
[18] R. Meng, G. Wu, J. Zhou, H. Zhou, H. Fang, M. A. Loi, and Y. Zhang, Chem. - Eur. J. **25**, 5480 (2019).
[19] L. Han, L. Wu, C. Liu, and J. Zhang, J. Phys. Chem. C **123**, 8578 (2019).
[20] J.-L. Li, J. Yang, T. Wu, and S.-H. Wei, J. Mater. Chem. C **7**, 4230 (2019).
[21] Y. Yamada, M. Hoyano, R. Akashi, K. Oto, and Y. Kanemitsu, J. Phys. Chem. Lett. **8**, 5798 (2017).
[22] P. K. Nayak, M. Sendner, B. Wenger, Z. Wang, K. Sharma, A. J. Ramadan, R. Lovrinčić, A. Pucci, P. K. Madhu, and H. J. Snaith, J. Am. Chem. Soc. **140**, 574 (2018).
[23] A. L. Abdelhady, M. I. Saidaminov, B. Murali, V. Adinolfi, O. Voznyy, K. Katsiev, E. Alarousu, R. Comin, I. Dursun, L. Sinatra *et al.*, J. Phys. Chem. Lett. **7**, 295 (2016).
[24] M. Khan, A. Mukhtar, N. Alwadai, M. Irfan, I.-u. Haq, H. Albalawi, A. Almuqrin, M. Almoneef, and M. Iqbal, Coatings **12**, 386 (2022).
[25] M. Khan, S. Yasmin, N. Alwadai, M. Irfan, Ikram-ul-Haq, H. Albalawi, A. H. Almuqrin, M. M. Almoneef, and M. Iqbal, Materials **15**, 5216 (2022).
[26] P. Giannozzi, O. Andreussi, T. Brumme, O. Bunau, M. Buongiorno Nardelli, M. Calandra, R. Car, C. Cavazzoni, D. Ceresoli, M. Cococcioni, N. Colonna, I. Carnimeo, A. Dal Corso, S. de Gironcoli, P. Delugas, R. A. DiStasio, Jr., A. Ferretti, A. Floris, G. Fratesi, G. Fugallo, R. Gebauer, U. Gerstmann, F. Giustino, T. Gorni, J. Jia, M. Kawamura, H.-Y. Ko, A. Kokalj, E. Küçükbenli, M. Lazzeri, M. Marsili, N. Marzari, F. Mauri, N. L. Nguyen, H.-V. Nguyen, A. Otero-de-la-Roza, L. Paulatto, S. Poncé, D. Rocca, R. Sabatini, B. Santra, M. Schlipf, A. P. Seitsonen, A. Smogunov, I. Timrov, T. Thonhauser, P. Umari, N. Vast, X. Wu, and S. Baroni, J. Phys.: Condens. Matter **29**, 465901 (2017).
[27] P. Giannozzi, S. Baroni, N. Bonini, M. Calandra, R. Car, C. Cavazzoni, D. Ceresoli, G. L. Chiarotti, M. Cococcioni, I. Dabo, A. Dal Corso, S. de Gironcoli, S. Fabris, G. Fratesi, R. Gebauer, U. Gerstmann, C. Gougoussis, A. Kokalj, M. Lazzeri, L. Martin-Samos, N. Marzari, F. Mauri, R. Mazzarello, S. Paolini, A. Pasquarello, L. Paulatto, C. Sbraccia, S. Scandolo, G. Sclauzero, A. P. Seitsonen, A. Smogunov, P. Umari, and R. M. Wentzcovitch, J. Phys.: Condens. Matter **21**(39), 395502 (2009).
[28] P. Giannozzi, O. Baseggio, P. Bonfà, D. Brunato, R. Car, I. Carnimeo, C. Cavazzoni, S. de Gironcoli, P. Delugas, F. Ferrari Ruffino, A. Ferretti, N. Marzari, I. Timrov, A. Urru, and S. Baroni, J. Chem. Phys. **152**, 154105 (2020).
[29] J. P. Perdew, K. Burke, and M. Ernzerhof, Phys. Rev. Lett. **77**, 3865 (1996).
[30] H. J. Monkhorst and J. D. Pack, Phys. Rev. B **13**, 5188 (1976).
[31] A. Walsh, elds22, F. Brivio, and J. M. Frost (2019). "Wmd-group/hybrid-perovskites: Collection 1," Zenodo. https://doi.org/10.5281/zenodo.2641358
[32] J. Heyd, G. E. Scuseria, and M. Ernzerhof, J. Chem. Phys. **118**, 8207 (2003).
[33] G. Pizzi, V. Vitale, R. Arita, S. Blügel, F. Freimuth, G. Géranton, M. Gibertini, D. Gresch, C. Johnson, T. Koretsune, J. Ibañez-Azpiroz, H. Lee, J.-M. Lihm, D. Marchand, A. Marrazzo, Y. Mokrousov, J. I. Mustafa, Y. Nohara, Y. Nomura, L. Paulatto, S. Poncé, T. Ponweiser, J. Qiao, F. Thöle, S. S. Tsirkin, M. Wierzbowska, N. Marzari, D. Vanderbilt, I. Souza, A. A. Mostofi, and J. R. Yates, J. Phys.: Condens. Matter **32**, 165902 (2020).
[34] N. Marzari and D. Vanderbilt, Phys. Rev. B **56**, 12847 (1997).
[35] I. Souza, N. Marzari, and D. Vanderbilt, Phys. Rev. B **65**, 035109 (2001).
[36] A. Damle, L. Lin, and L. Ying, J. Chem. Theory Comput. **11**, 1463 (2015).
[37] A. Damle and L. Lin, Multiscale Model. Simul. **16**, 1392 (2018).
[38] E. Runge and E. K. U. Gross, Phys. Rev. Lett. **52**, 997 (1984).
[39] D. Rocca, "Time-dependent density functional perturbation theory: New algorithms with applications to molecular spectra," Ph.D. Thesis, SISSA, 2007, https://hdl.handle.net/20.500.11767/3936.
[40] I. Timrov, "Ab initio study of plasmons and electron-phonon coupling in bismuth: From free-carrier absorption towards a new method for electron energy-loss spectroscopy," Ph.D. thesis, Ecole Polytechnique X, 2013.
[41] E. K. U. Gross and W. Kohn, Phys. Rev. Lett. **55**, 2850 (1985).
[42] C. Freysoldt, B. Grabowski, T. Hickel, J. Neugebauer, G. Kresse, A. Janotti, and C. G. Van de Walle, Rev. Mod. Phys. **86**, 253 (2014).
[43] A. A. Emery and C. Wolverton, Sci. Data **4**, 170153 (2017).
[44] J. L. Lyons, Chem. Mater. **33**, 6200 (2021).
[45] J. Guo, J. Zhang, Y. Di, and Z. Gan, Nanomaterials **14**, 683 (2024).
[46] M. Arya, P. Bhumla, S. Sheoran, and S. Bhattacharya, Phys. Chem. Chem. Phys. **26**, 10419 (2024).
[47] M. Chaudhary, A. Karmakar, V. Mishra, A. Bhattacharya, D. Mumbaraddi, A. Mar, and V. K. Michaelis, Commun. Chem. **6**, 75 (2023).
[48] F. P. Sabino, A. Zunger, and G. M. Dalpian, Mater. Horiz. **9**, 791 (2022).
[49] E. Jedlicka, J. Wang, J. Mutch, Y.-K. Jung, P. Went, J. Mohammed, M. Ziffer, R. Giridharagopal, A. Walsh, J.-H. Chu, and D. S. Ginger, J. Phys. Chem. Lett. **12**, 2749 (2021).
[50] F. M. Rombach, L. Gregori, A. Sidler, J. Whitworth, S. Zeiske, H. Jin, E. Y.-H. Hung, S. Motti, P. Caprioglio, A. Armin *et al.*, J. Mater. Chem. C **13**, 5161 (2025).
[51] S. Maqsood, A. U. Rahman, M. Nawaz, M. A. Ahmad, M. Manzoor, N. A. Noor, and S. A. M. Abdelmohsen, J. Mater. Res. Technol. **17**, 649 (2022).
[52] E. Mosconi, B. Merabet, D. Meggiolaro, A. Zaoui, and F. De Angelis, J. Phys. Chem. C **122**, 14107 (2018).
[53] G. Volonakis, A. A. Haghighirad, R. L. Milot, W. H. Sio, M. R. Filip, B. Wenger, M. B. Johnston, L. M. Herz, H. J. Snaith, and F. Giustino, J. Phys. Chem. Lett. **8**, 772 (2017).
[54] B. Al-Anesi, G. K. Grandhi, A. Pecoraro, V. Sugathan, N. S. M. Viswanath, H. Ali-Löytty, M. Liu, T.-P. Ruoko, K. Lahtonen, D. Manna *et al.*, Small **19**, 2303575 (2023).
[55] D. Meggiolaro, S. G. Motti, E. Mosconi, A. J. Barker, J. Ball, C. Andrea Riccardo Perini, F. Deschler, A. Petrozza, and F. De Angelis, Energy Environ. Sci. **11**, 702 (2018).